www.vbripress.com/aml, DOI: 10.5185/amlett.2016.6297 Published online by the VBRI Press in 2016

Chunk shaped ZnO/Co_3O_4 nanocomposites for ethanol sensor

C. Stella*, N. Soundararajan, K. Ramachandran

School of Physics, Madurai Kamaraj University, Madurai 625021, India

*Corresponding author. Tel.: (+91) 7708138350; E-mail: stellachandran89@gmail.com

Received: 13 November 2015, Revised: 20 January 2016 and Accepted: 20 May 2016

ABSTRACT

Chunk shaped ZnO/Co_3O_4nanocomposites for different concentrations of 90:10 (Z9C1), 70:30 (Z7C3), and 50:50 (Z5C5) were successfully synthesized by co-precipitation method. The structure, morphology, and elemental composition of the prepared samples were characterized by X-ray diffraction (XRD), scanning electron microscopy (SEM), and energy dispersive spectroscopy (EDS), respectively which confirm the formation of ZnO/Co_3O_4nanocomposites. Raman analysis confirmed the presence of oxygen vacancies in the Z5C5 sample. The magnetic studies revealed that, the Z5C5 nanocomposite exhibit room temperature ferromagnetism. The gas sensing property clearly confirm the response of Z5C5 sensor which was as high as 5.6%, about 4 times higher than Z9C1 sample. The enhancement of gas sensing property is due to the collective contribution of smaller particle size, oxygen vacancies, and the formation of more p-n hetero junction in Z5C5 nanocomposite.

Keywords: ZnO/Co_3O_4; nanocomposites; chunk shape; ethanol sensor; fiber-optic technique.

Introduction

Extensive research is being carried out for the development of selective and sensitive gas sensors for diverse applications in the fields of, air quality detection, inflammable-gas inspection, environmental monitoring, energy optimization, food, health and security [**1-3**]. Oxide semiconductor gas sensors are widely investigated due to their high sensitivity, cost effectiveness, and reliability [**4-8**]. The sensitivity of the sensor is influenced by many factors, and the sensitivity is enhanced by surface modification, doping with noble metals (Pt, Pd, Au, and Ag), and composite formation, etc., [**9-12**]. The nanocomposite formed from p- and n- type semiconducting oxides would combine the intrinsic properties of individual components [**13-15**]. The junctions formed by p- and n-type semiconductors provide a range of valuable applications such as, diodes, transistors, solar cells, gas sensors, and light emitting diodes [**16-18**]. In gas sensing applications, the combination of p- and n- type nanomaterial can provide higher sensitivity due to the formation of the extended depletion layer [**19**]. So far, attempts have been made on the development of n-type semiconducting metal oxide-based gas sensors. Among them, ZnO is an ideal candidate for gas sensor because of its excellent characteristics such as, low cost, high sensitivity, rapid response, fast recovery, and high mobility of conduction electrons [**20-23**]. Recently, Mishra *et al*. [**24**] prepared the ZnO tetrapod by flame transport synthesis approach. The porous nature of tetrapod and large number of junctions between the branches of tetrapod offers more active centers, which leads to enhanced sensing towards H_2 gas. Few works have dealt with p-type semiconducting oxide-based gas sensors [**25, 26**]. The most promising p-type materials for gas sensing applications are, Co_3O_4, CuO, NiO, and Cr_2O_3, which showed quite promising sensing properties for rapid and reliable detection of C_3H_6O, C_2H_5OH, NH_3, H_2, CO, NO_2, and H_2 gases. Among the p-type semiconductors, Co_3O_4 is one of the most interesting prospects because it has several potential applications such as, in catalysts, electrode materials in Li-ion batteries, magnetism, and especially gas sensors [**25-28**]. In particular, the oxidative catalytic activity of Co_3O_4 is well-known, and can be used to enhance the gas response. Indeed, several studies showed improved gas-sensing characteristics by the addition of Co_3O_4 to the n-type semiconductors [**29, 30**].

Sun *et al.* [**31**] studied the gas sensing characteristics of n-type WO_3 and p-type Cr_2O_3composite at 300 °C, which showed selective detection towards NO gas due to the formation of interface between two oxides. Lupan *et al.* [**32**] observed the improved response and recovery time for Zn-doped CuO, and the p-p hetero structure formed between CuO/Cu_2O enhance the ethanol gas response behavior. Xue *et al*. [**33**] prepared the CuO/SnO_2 core shell p-n junction nanorods by hydrothermal method and showed higher sensitivity and selectivity towards H_2S. Hazra *et al*. [**34**] reported the hydrogen sensitivity of ZnO p-n homo junctions. Choi *et al.* [**29**] worked on the SnO_2-Co_3O_4 composite to detect CO and H_2. Dandeneau *et al*. [**16**] prepared p-CuO/n-ZnOheterocontact thin films through spin coating method and found that they exhibited higher sensitivity. Na *et al*. [**30**] observed selective detection toward NO_2 and C_2H_5OH using Co_3O_4 decorated ZnO nanowires. Park *et al*. [**35**] suggested that the formation of p-n junction in ZnO/Co_3O_4 was responsible for the

enhanced response and selectivity towards NO_2 gas, when compared with pure ZnO. Since upon exposure to NO_2 the depletion and accumulation layer in the interface region become thicker and the potential barrier height at the interface increases, which leads to increase in the resistance. Thus, the hetero structures between p-type Co_3O_4 and n-type ZnO can provide valuable platform for high performance gas sensors.

In this context, the present work is focused on the preparation of ZnO/Co_3O_4 nanocomposites for ethanol sensing by fiber optic method. Generally, the sensitivity of ZnO/Co_3O_4nanocomposite is examined on the basis of change in electrical properties (resistance, conductance, etc.) of the material. But, when a metal oxide semiconductor is exposed to the target gas, both electrical and optical properties of the material are liable to change. Fiber optic sensor works on the principle of change in optical properties, which offers many advantages over conventional resistive-type sensors because of their light weight, small dimension, low cost, immunity to electromagnetic interference and corrosion, and multiplexing capabilities [**36**]. Using a clad modified fiber optic sensor, Mariammal *et al*. [**37**] studied CuO modified SnO_2 toward ethanol. In our earlier work, we studied the ethanol sensing of Mn-doped Co_3O_4nanorods by fiber optic method [**38**]. In this work, we made a new attempt of ethanol sensing by ZnO/Co_3O_4 nanocomposite using fiber optic method.

Experimental

Synthesis of ZnO/Co_3O_4 nanocomposites

Co-precipitation method was employed to prepare ZnO/Co_3O_4 (90:10, 70:30, 50:50) nanocomposites. In a typical synthesis process of nanocomposite (90:10), 0.2 M of zinc nitrate hexahydrate ($Zn(NO_3)_2.6H_2O$) was dissolved in 250 ml of distilled water. The appropriate amount of cobaltous nitrate hexahydrate ($Co(NO_3)_2.6H_2O$) was added into the Zn precursor solution, and the solution was stirred for half an hour. Then, 250 ml of aqueous solution of oxalic acid (0.4 M) was added drop wise into the above solution under constant stirring. The resultant solution was stirred for 12 h at room temperature (RT). The precipitate obtained was centrifuged, washed subsequently several times with distilled water and ethanol in order to remove the unreacted ions, and then dried in air at 100 °C. ZnO/Co_3O_4 nanocomposites were obtained when the dried powder was annealed at 700 °C in a muffle furnace. For the synthesis of (70:30), and (50:50) nanocomposite the concentration of Zinc and Cobalt precursors were varied. The synthesized samples were labeled as, Z9C1 (90:10), Z7C3 (70:30), and Z5C5 (50:50).

Characterizations

X-ray diffraction (XRD) measurements of the samples were done by X-ray diffractometer (Bruker D8 Advance) with Cu-Kα as the radiation source (wavelength: 1.54056 Å). The morphology of the samples was analyzed by scanning electron microscope (SEM, VEGA 3 TESCAN) operating at an accelerating voltage of 30 kV. The elemental analysis was carried out by energy dispersive spectroscopy (EDS, Bruker). Fourier transform infrared (FT-IR) spectra were obtained using the KBr method on a Fourier transform infrared spectrometer (Shiraz) at RT in the wavelength range of 4000 – 400 cm^{-1} with a resolution of 1 cm^{-1}. Micro-Raman spectra were recorded at RT using LABRAM HR visible (400-1100 nm) model with a 632.8 nm excitation source of He-Ne laser. The RT photoluminescence (PL) spectra were recorded by using spectroflurophotometer (Shimadzu RF-5000). The magnetization measurements were done by vibrating sample magnetometer (VSM) (Lake Shore, 7404). The ethanol sensitivity was examined using fiber-optic sensor setup as previously reported [**39**].

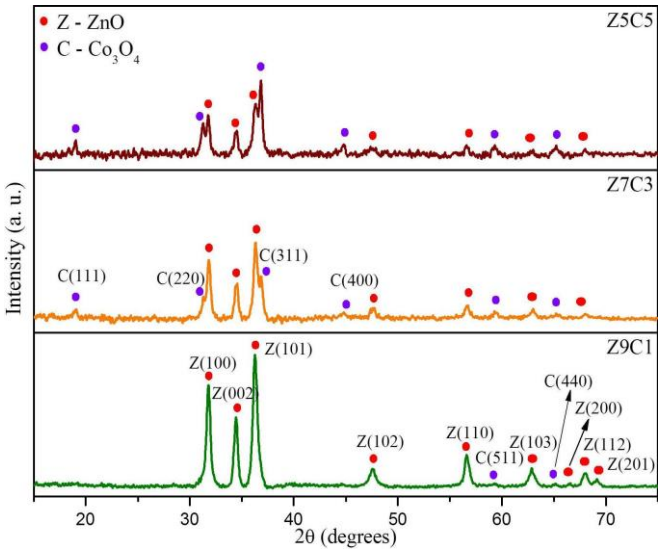

Fig. 1. XRD pattern of Z9C1, Z7C3, and Z5C5 nanocomposites.

Results and discussion

X-ray diffraction analysis

Fig. 1 shows the XRD pattern of the synthesized ZnO/Co_3O_4 nanocomposites. For the Z9C1 nanocomposite, the apparent peaks appeared at 2θ values 31.79°, 34.43°, 36.26°, 47.53°, 56.62°, 62.86°, 66.59°, 68.06°, and 69.11° correspond to the crystal planes of (100), (002), (101), (102), (110), (103), (200), (112), and (201), respectively which confirms the formation of pure hexagonal wurtzite ZnO (JCPDS card NO. 89-0510). In addition to these peaks in the same spectra, two peaks appeared at 2θ values of 59.24° and 65.10° correspond to the crystal planes of (511) and (440), respectively which confirms the formation of pure cubic Co_3O_4 (JCPDS card NO. 65-3103). Further, the XRD pattern of Z7C3 and Z5C5 shows the extra peaks at 2θ values of 19.06°, 31.31°, 36.85°, and 44.82°, which correspond to cubic Co_3O_4 crystal planes of (111), (220), (311), and (400), respectively. The coexistence of both Co_3O_4 and ZnO phase confirms the formation of junction between p-type Co_3O_4 and n-type ZnO [**19**]. Overall, results confirm the formation of ZnO/Co_3O_4nanocomposite. The intensity of Co_3O_4 reflections underwent an enhancement upon increasing the corresponding Co content; simultaneously ZnO reflections underwent reduction upon decreasing the corresponding Zn content. It is worthwhile to notice that no additional reflections or peaks shifts suggesting the presence of ternary phases we ever detected.

By using Scherrer's equation, the crystallite size and the lattice parameters of ZnO and Co_3O_4 are estimated and are presented in **Table 1a**. In addition to this, the preferred orientation of ZnO and Co_3O_4 can be obtained from the texture coefficient (T_c). T_c has been calculated by using the formula,

$$T_{c(hkl)} = \frac{I_{(hkl)} / I_{0(hkl)}}{(1/N)\left[\sum_N I_{(hkl)} / I_{0(hkl)}\right]}$$

where, $T_{c(hkl)}$ is the texture coefficient of the hkl plane, $I_{(hkl)}$ is the measured intensity, $I_{0(hkl)}$ is the relative intensity of the corresponding hkl plane given in JCPDS, and N is number of reflections. T_c for the predominant ZnO planes (100), (002), (101), and Co_3O_4 planes (111), (220), (311) are calculated and tabulated in **Table 1b**. If $T_c \approx 1$, the nanoparticles are with randomly oriented crystallite, while, $T_c > 1$ abundance of grain in a given (hkl) direction, and if $T_c < 1$ lack of grain in that direction [**40**]. The (002) and (111) planes have the highest value of T_c for ZnO and Co_3O_4, respectively, and T_c for (311) plane is less than 0.5, so it is negligible. The value of T_c for ZnO decreases as the concentration of Co_3O_4 increases. The texture analysis thus indicates that the composite materials Z7C3 and Z5C5 are highly textured along (111) plane. However, with the increasing concentration of Co_3O_4 the texture coefficient of (111) plane increases remarkably with concomitant decrease in (220) plane which results in reduced planar density on (220) plane. The atomic planar density of (111) planes increases at the cost of (220) plane which results in the creation of oxygen vacancies on (220) plane. Kumar *et al*. [**41**] also observed this type of results in W-doped SnO_2 with the reduction of texture coefficient along (110) plane with the concomitant increase along loosely packed (200) planes and which have prominent effect on gas sensing property.

Table 1a. Crystallite size and lattice parameters.

Samples	Crystallite size (nm)		Lattice parameters (Å)		
	ZnO	Co_3O_4	ZnO		Co_3O_4
			a	c	a
Z9C1	17	-	3.2452(1)	5.2081(3)	-
Z7C3	16	21	3.2443(1)	5.1951(4)	8.0849(3)
Z5C5	9	8	3.2491(1)	5.2005(4)	8.0843(3)

Table 1b. Texture coefficient for different planes.

Samples	ZnO			Co_3O_4		
	$T_{c(100)}$	$T_{c(002)}$	$T_{c(101)}$	$T_{c(111)}$	$T_{c(220)}$	$T_{c(311)}$
Z9C1	1.255	1.355	0.895	-	-	-
Z7C3	1.114	1.330	0.705	3.375	1.076	0.271
Z5C5	0.951	1.134	0.555	3.382	0.794	0.269

SEM with EDS analysis

Fig. 2 shows the SEM micrographs of Z9C1 (a-c) and Z5C5 (d-f) samples. The SEM images of both Z9C1 and Z5C5 samples show chunk-shaped morphology [**42,43**]. Variation in the ZnO and Co_3O_4 concentration doesn't change the morphology. It seems that stack of nanorods are arranged side by side to form a bundle. This type of structure formed due to agglomeration of the particles, since the reaction time was high and also the agglomeration effect was very prominent in aqueous media. The chemical composition of the samples is very essential to know the exact concentration of elements in the samples. The EDS spectra of Z9C1 and Z5C5 samples are also shown in **Fig. 2 (g** and **h)**. Both the samples reveal the presence of Zn, Co, and O elements alone in the sample, confirming the absence of any other impurities. The atomic percentage of oxygen in Z9C1 and Z5C5 samples are 57.98 and 50.85%, respectively, which shows the oxygen deficiency in the Z5C5 sample.

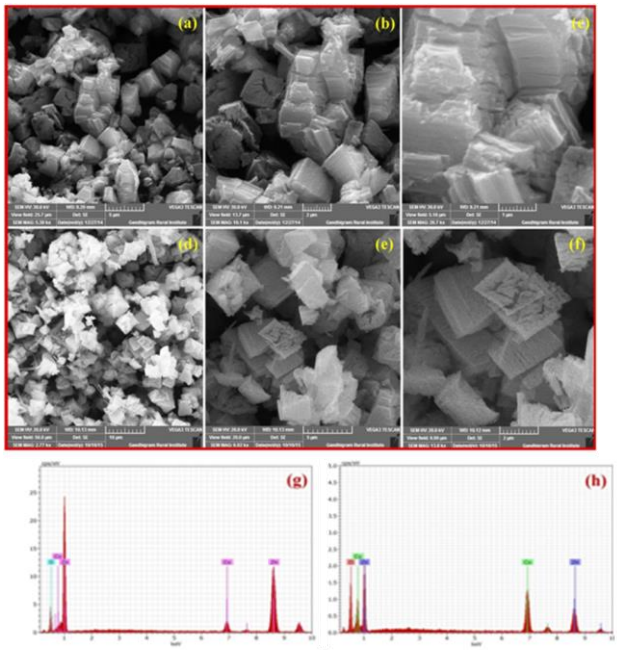

Fig. 2. SEM micrograph and EDS spectra of (a,b,c,g) Z9C1, (d,e,f,h) Z5C5 nanocomposites, respectively.

FTIR analysis

FTIR spectra of ZnO/Co_3O_4nanocomposites are shown in **Fig. 3(a)**. For all the samples, the E1 transverse optical mode of ZnO is present at 420 cm^{-1} [**44**]. Furthermore, two other bands at 569 and 668 cm^{-1} are observed due to Co_3O_4 stretching modes, where the first band is associated with OB_3 vibration in the spinel lattice and second band with the ABO_3 vibration, where, A and B denotes the Co^{2+} ($3d^7$) in tetrahedral site and Co^{3+} ($3d^6$) in an octahedral site, respectively [**28**]. Notably, the intensity of the bands increases as a function of Co_3O_4 concentration. FTIR spectra confirmed the co-presence of ZnO and Co_3O_4 and ruling out the formation of ternary phase in the synthesized samples. The broad bands observed around 3443 and 1629 cm^{-1} are due to the presence of O-H stretching and bending modes of the hydroxyl group, respectively. The band observed at 2364 cm^{-1} is due to CO_2 molecule in air.

Raman analysis

The Raman spectra of ZnO/Co_3O_4nanocomposites are shown in **Fig. 3(b)**. For Z9C1, the mode at 432 cm^{-1} corresponds to E_2(H) mode, which is the characteristic peak

of hexagonal wurtzite ZnO phase. The peak at 322 cm^{-1} is due to multiple phonon scattering process ($E_2(H)$-$E_2(L)$) [**45**]. The modes around 478, 526, 686 cm^{-1} are due to E_g, F_{2g}, A_{1g} phonon symmetries of Co_3O_4, in which Co^{2+} and Co^{3+} cations situated at tetrahedral and octahedral sites undergoing lattice vibration in the cubic lattice, confirming the presence of spinel Co_3O_4 [**28**].

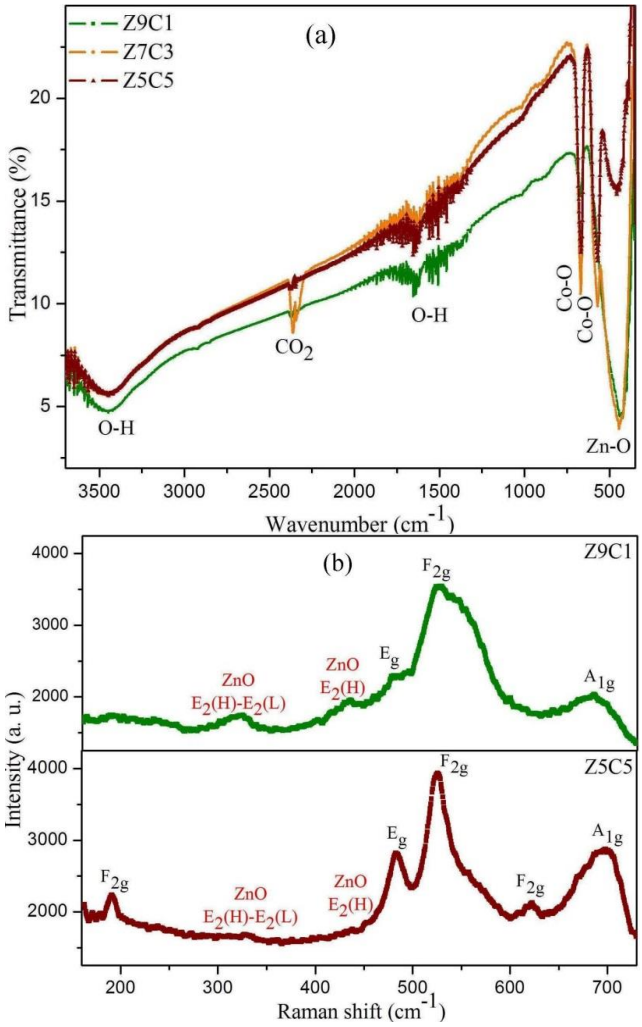

Fig. 3. (a) FTIR and (b) Raman spectra of ZnO/Co_3O_4nanocomposites.

The Raman spectra again confirm the formation of wurtzite ZnO and cubic Co_3O_4 in the composite material, which further testifies the results of XRD data. In the case of Z5C5 sample, the peaks at 191 and 623 cm^{-1} correspond to $2F_{2g}$ modes of Co_3O_4. With the increasing concentration of Co_3O_4, all the modes are shifted towards higher wavenumber due to the composite formation. In addition, the intensity of Co_3O_4 modes increases and ZnO modes decreases. The decrease in intensity of $E_2(H)$ mode confirms the increase of oxygen vacancies, because this mode is associated with oxygen atoms [**46,47**]. Similarly, the oxygen vacancy related defects are observed in the photoluminescence spectra presented in the supporting information (**Fig. S1**). The intensity of oxygen vacancy mode is high for Z5C5 sample which confirms the formation of more number of oxygen vacancies in the sample. Since the oxygen vacancies play a significant role in the gas sensing mechanism, Z5C5 sample is expected to show better sensitivity.

VSM analysis

Magnetization versus applied magnetic field curves were measured for the three composites at RT. **Fig. 4** shows the hysteresis behavior of ZnO/Co_3O_4nanocomposites. The Z9C1 and Z7C3 samples show the characteristic patterns of both diamagnetic and ferromagnetic components. The diamagnetic component is inferred from the negative slope at high magnetic fields and ferromagnetic component from the hysteresis behavior at low magnetic field. Both these samples possess coercivity (H_c) and remanance (M_r) as can be seen from the hysteresis loops on the expanded scale given in the bottom inset of **Fig. 4**. In the case of Z5C5 sample, a pure ferromagnetic behavior is observed from the curve. The hysteresis loop of Z5C5 does not show any tendency to saturate even at a high magnetic field of 12 KOe, indicating the presence of antiferromagnetic component along with ferromagnetic phase. Despite the diamagnetic character of ZnO and the antiferromagnetic behavior of Co_3O_4 exhibit ferromagnetic behavior when they combine together. Martin-Gonzalez *et al.* [**48**] observed the room temperature ferromagnetism (RTFM) in ZnO/Co_3O_4 mixture, and the presence of RTFM can be understood from the core-shell model in which antiferromagnetic Co_3O_4 is surrounded by a CoO like shell, which promote the interaction of Co^{2+} ions in Co_3O_4 and CoO. Serrano *et al.* [**49**] also observed RTFM in TiO_2/Co_3O_4 mixture, which is due to the reduction of Co^{3+} ions of Co_3O_4 in octahedral positions to Co^{2+} when interacts with TiO_2. The observed RTFM in Z5C5 sample might be attributed to different origins. One possible source of ferromagnetism in ZnO/Co_3O_4nanocomposite is, the metallic Co.

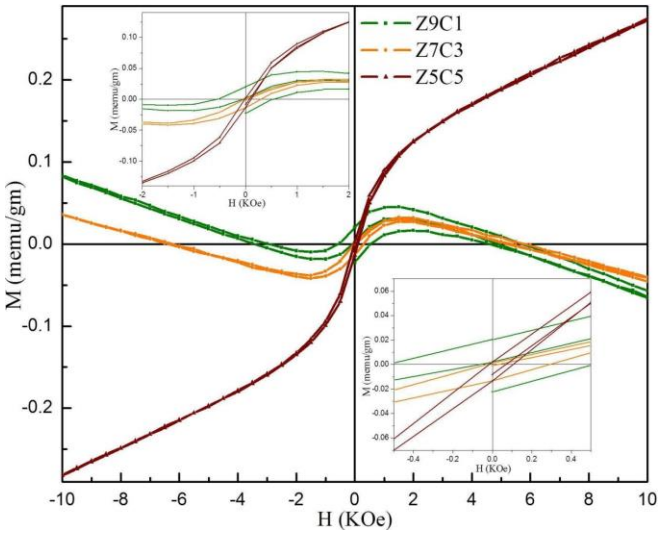

Fig. 4. M(H) curves for Z9C1, Z7C3, and Z5C5 nanocomposites measured at RT. The hysteresis loops at low magnetic fields are given in the top inset. The bottom inset shows the curves on the expanded scale.

However, the XRD results have not shown any evidence of cobalt metal in the composite, eliminating it as a contributing factor to the magnetic properties. Thus, the second possibility is that the Co^{2+} cations play a main role in

the ferromagnetism. However, no CoO peaks have been observed in the XRD spectra. The presence of RTFM in Z5C5 may due to partial replacement of Zn^{2+} and Co^{2+} on the surface of Co_3O_4. The non-magnetic Zn^{2+} ions change the equality of the antiparallelly aligned Co^{2+} magnetic moments [**50**]. Further the RTFM also due to bound magnetic polaron (BMP). BMP are formed when the charge carriers bound to the oxygen vacancies leading to magnetic polarization. In our earlier work, we demonstrated the RTFM in Co-doped TiO_2 and also, there is a direct relationship between the magnetization, sensing, and the relative occupancy of the oxygen vacancy present on the surface of the nanoparticles [**51**]. Hence, it is expected that when FM exists due to oxygen vacancies, then it can enhance the sensing performance.

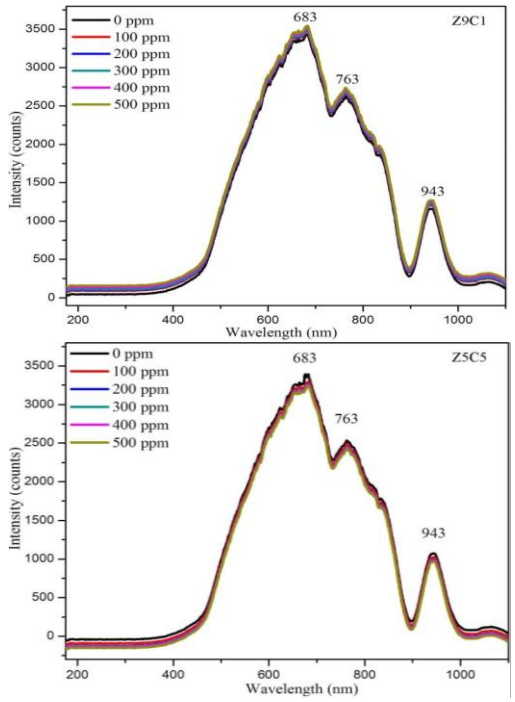

Fig. 5. Spectral response of Z9C1 and Z5C5 nanocomposites towards ethanol at RT.

Ethanol sensing properties

Spectral response of ZnO/Co_3O_4 nanocomposites: The ethanol sensing properties of ZnO/Co_3O_4 nanocomposite was investigated for various concentration of ethanol using clad modified fiber optic technique. The ethanol concentration was increased from 0-500 ppm in steps of 100 ppm. The spectral response of Z9C1 and Z5C5 are presented in **Fig. 5.** The spectra show three characteristic peaks of optical fiber around 683, 763, and 943 nm and the relative peak intensity is higher around 683 nm when compared to the other maxima. Sensitivity is defined as the change in peak intensity to the change in gas concentration and the sensitivity is found for high intensity peak at the wavelength of 683 nm. **Fig. 6** shows the variation of sensitivity at 683 nm with a concentration of ethanol and the sensitivity is found to be 1.4 and 5.6% for 100 ppm of ethanol for Z9C1 and Z5C5, respectively.

Gas sensing mechanism: In a fiber optic sensor, the gas sensing mechanism occurs at the surface of modified cladding (sensing material). When a sensing material is exposed to air, oxygen molecules in the atmosphere adsorbed on the surface of the sensing material to form O_2^-, O^- and O^{2-} by trapping electrons from the conduction band, which depending on the temperature in air. The stable oxygen ions are, O_2^- below 150 °C, O^- between 150 and 400 °C, and O^{2-} above 400 °C. Since here the measurements are carried out at RT, the O_2^- ions play a crucial role in surface reactions. When ethanol gas is passed, ethanol molecules react with pre-adsorbed oxygen ions releasing the trapped electrons back to the semiconductor with the formation of CO_2 and H_2O. The changes in carrier concentration change the optical properties of the sensing material. Here, the fiber optic sensor works on the principle of leaky mode [**38**]. Since from the earlier reports by our group, the refractive indices of ZnO (n_{ZnO} = 2.34) [**52**] and Co_3O_4 (n_{Co3O4} = 2.62) [**38**] are greater than that of core (n_{core} = 1.492). Under this situation, the condition for total internal reflection violated at the core-clad interface. But, some of the refracted light is adsorbed by the sensing material depending on the absorption coefficient of the sensing materials. At the modified clad-air interface, the condition for total internal reflection is satisfied, since the refractive index of air (n_{air} = 1) is less than the sensing materials. The evanescent field that occurs at this interface is absorbed by the air and ethanol molecules affecting the intensity of the guided signal [**39**]. Hence, the intensity of the guided signal is affected by the attenuation of both the refracted ray and evanescent field.

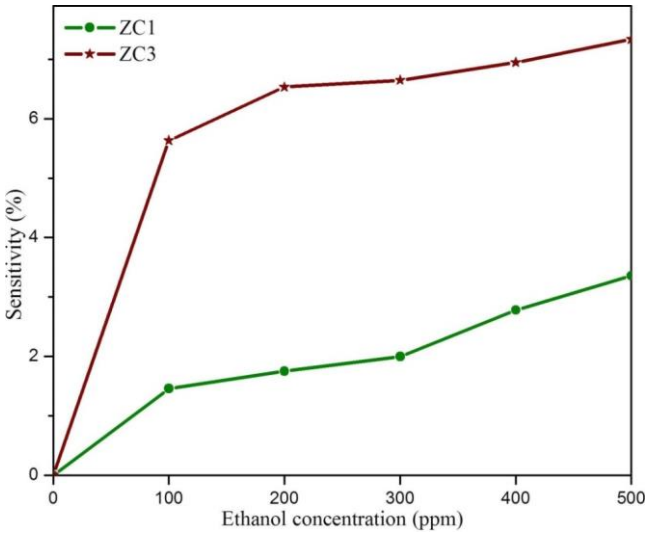

Fig. 6. Variation of sensitivity with ethanol concentration for Z9C1 and Z5C5 nanocomposites at RT.

When ZnO/Co_3O_4 is exposed to analyte, the oxygen species on Co_3O_4 promote the oxidation of ethanol molecules to CO_2 and H_2O and the release of electrons which could change the carrier concentration. In ZnO/Co_3O_4, the formation of p-n junction between p-type Co_3O_4 and n-type ZnO contribute to the sensitivity. At the p-n heterojunctions, oxygen deficient ZnO has shown n-type carriers with electrons, whereas oxygen excess Co_3O_4 shows p-type carriers by holes. The heterojunction region of ZnO/Co_3O_4 is easily attracting the reducing/oxidizing gases, thus forming deeper electron

depletion layer. In addition to the existence of p-n heterojunctions, the enhanced sensing performance of the ZnO/Co_3O_4 composite sensor might be partly due to the prominent catalytic property of Co_3O_4. A large amount of oxygen is known to be adsorbed on the surface of Co_3O_4. Higher sensitivity is observed for Z5C5 sample when compared with Z9C1. This is because the Z5C5 sample contains more Co_3O_4 nanoparticles than Z9C1. Similar result was observed by Na *et al*. [**30**] in the Co_3O_4-decorated ZnO nanowires. The sensitivity and selectivity towards NO_2 and ethanol were enhanced by the catalytic effect of Co_3O_4, and the extension of the electron depletion layer using the p-n junction. The sensing measurement for Pure ZnO is given in the supporting information (**Fig. S2**). The sensitivity of pure ZnO (0.8%) is low when compared with the composite materials. Since when ZnO is exposed to air oxygen species adsorbed on the surface of ZnO, through capturing the electrons from the conduction band. Thus, an electron depletion layer is built near the surface of ZnO. Once the ZnO gas sensor contacted with the ethanol, the captured electrons will return to ZnO conduction band, resulting in a reduced electron depletion layer. Zhang *et al*. [**19**] also worked on the ZnO/Co_3O_4 microspheres for ethanol gas sensing at 275 °C, and observed five-fold increased sensitivity in ZnO/Co_3O_4 compared with ZnO. The enhanced sensitivity was attributed to the porous nature of the material and also the formation of p-n junction.

Table 2. Comparison of sensing performance toward ethanol.

Sample	Operating temperature (°C)	Concentration (ppm)	Sensitivity
Co_3O_4/ZnO nanoparticles [**53**]	170	100	46
pyramid like Co_3O_4/ZnO nanoparticles morphology [**54**]	400	100	30
MesoporousZnO/Co_3O_4 microspheres [**19**]	275	50	41
Co_3O_4 decorated ZnO nanowire [**30**]	400	100	22
Co_3O_4 loaded SnO_2 [**55**]	300	1000	301
ZnO/SnO_2 nanoparticles [**17**]	RT	100	2.5
ZnOnanorods [**52**]	RT	100	3.8
Co_3O_4nanorods [**38**]	RT	100	1.6
Chunck shaped ZC1	RT	100	1.4
ZnO/Co_3O_4nanocomposite (Present work) ZC3	RT	100	5.6

A comparison of response of present sensor with the reported sensors in the literature is given in **Table 2**. Most of the sensors showed high sensitivity at high operating temperature, but in this work the sensor performance of ZnO/CO_3O_4 is studied at RT. The optical method is highly reliable than conventional resistive method since the change in optical properties is more sensitive compared to the change in the resistance even at RT. The sensitivity of ZnO/Co_3O_4nanocomposite in this work is comparably higher than the pure ZnO and Co_3O_4 by fiber optic method. Thus, ZnO/Co_3O_4nanocomposite is highly promising in detecting ethanol gas at RT with good sensitivity.

Conclusion

Thus, in conclusion, the ethanol sensing by chunk shaped ZnO/Co_3O_4nanocomposites were investigated by fiber optic technique at RT. ZnO/Co_3O_4nanocomposites were synthesized via simple co-precipitation method. The presence of both hexagonal wurtzite ZnO and cubic Co_3O_4 in the composite material was confirmed by XRD. The texture analysis indicated that the composite materials were textured along (111) plane. The texture coefficient of (111) plane increases at the expense of (220) plane. Reduction in texture coefficient of (220) plane creates vacancies for adsorption of ethanol molecules, reflected in higher sensing response of Z5C5. The Raman spectroscopy confirmed the formation of ZnO/Co_3O_4nanocomposite and also the presence of oxygen vacancies in the Z5C5 sample. The presence of RTFM in Z5C5 sample attributed to the partial replacement of Zn^{2+} with Co^{2+} ions and also the presence of oxygen vacancies. Compared to Z9C1 sample, Z5C5 sample showed better response due to the smaller particle size, oxygen vacancies, catalytic activity of Co_3O_4, and the formation of more hetero junctions. From the study, it is concluded that ZnO/Co_3O_4nanocomposites have potential application in detecting ethanol.

Acknowledgements

One of the authors (KR) acknowledges CSIR, New Delhi for the award of Emeritus Scientist Scheme. The authors would like to thank Dr. Vasant Sathe and Dr. Mukul Gupta, Scientist, UGC-DAE Consortium for Scientific Research, Indore for Raman and XRD measurements, Dr. D. Sastikumar and his scholar Mr. S. Devendiran, NIT, Trichy for sensor measurements.

Author's contributions

Conceived the plan: CS, KR; Performed the expeirments: CS; Data analysis: CS, NS, KR; Wrote the paper: CS. Authors have no competing financial interests.

Reference

1. Zhang, J.; Liu, X.; Neri, G.; Pinna, N.; *Adv. Mater*. **2015**. **DOI:** 10.1002/adma.201503825.
2. Meng, X.; Kim, S.; Puligundla, P.; Ko. S.; *J. Korean Soc. Appl. Bi.*, **2014,** 57, 723. **DOI:** 10.1007/s1378-014-4180-3.
3. Lupan, O.; Cretu, V.; Deng, M.; Gedamu, D.; Paulowicz, I.; Kaps, S.; Mishra, Y.K.; Polonskyi, O.; Zamponi, C.; Kienle, L.; Trofim, V.; Tiginyanu, I.; Adelung, R.; *J. Phys. Chem. C***2014**, 118, 15068. **DOI:** 10.1021/jp5038415.
4. Lupan, O.; Braniste, T.; Deng, M.; Ghimpu, L.; Paulowicz, I.; Mishra, Y.K.; Kienle, L.; Adelung, R.; Tiginyanu, I.; *Sens. Actuators B,***2015,** 221, 544. **DOI:** 10.1016/j.snb.2015.06.112.
5. Gedamu, D.; Paulowicz, I.; Kaps, S.; Lupan, O.; Wille, S.; Haidarschin, G.; Mishra, Y.K.; Adelung, R.; *Adv. Mater.***2014**, 26, 1541.
6. Paulowicz, I.; Hrkac, V.; Kaps, S.; Cretu, V.; Lupan, O.; Braniste, T.; Duppel, V.; Tiginyanu, I.; Kienle, L.; Adelung, R.; Mishra, Y.K.; *Adv. Elect. Mater.***2015**. **DOI:** 10.1002/aelm.201500081.
7. Comini, E.; Faglia, G.; Sberveglieri, G.; *Appl. Phys. Lett.*, **2002**, 81, 1869. **DOI:** 10.1063/1.1504867.
8. Wetchakun, K.; Samerjai, T.; Tamaekong, N.; Liewhiran, C.; Siriwong, C.; Kruefu, V.; Wisitsoraat, A.; Tuantranont, A.; Phanichphant, S.; *Sens. Actuators B,***2011,** 160, 580. **DOI:** 10.1016/j.snb.2011.08.032.
9. Wang, C.; Yin, L.; Zhang, L.; Xiang, D.; Gao, R.; *Sensors*, **2010,** 10, 2088. **DOI:** 10.3390/s100302088.
10. Basu, S.; Basu, P.K.; *J. Sensors*, **2009,** 861968, 20. **DOI:** 10.1155/2009/861968.
11. Shukla, S.K.; Vamakshi; Minakshi; Bharadavaja, A.; Shekhar, A.; Tiwari, A.; *Adv. Mat. Lett*. **2012**, 3, 421. **DOI:** 10.5185/amlett.2012.5349.

12. Song, X.; Wang, Z.; Liu, Y.; Wang, C.; Li, L.; *Nanotechnology*, **2009**, 20,075501. **DOI:** 10.1088/0957-4484/20/7/075501.
13. Bai, J.; Wang, K.; Feng, J.; Xiong, S.; *ACS Appl. Mater. Interfaces*,**2015**, 7, 22848. **DOI:** 10.1021/acsami.5b05303.
14. Yoo, Y.Z.; Fukumura, T.; Jin, Z.; Hasegawa, K.; Kawasaki, M.; *J. Appl. Phys.***2001**, 90, 4246. **DOI:** 10.1063/1.1402142.
15. Liu, L.; Zhao, C.; Zhao, H.; Zhang, Q.; Li, Y.; *Electrochim. Acta*, **2014**, 135, 224. **DOI:** 10.1016/j.electacta.2014.05.001.
16. Dandeneau, C.S.; Jeon, Y.H.; Shelton, C.T.; Plant, T.K.; Cann, D.P.; Gibbons, B. J.; *Thin Solid Films*,**2009,** 517, 4448. **DOI:** 10.1016/j.tsf.2009.01.054.
17. Mariammal, R.N.; Stella, C.; Renganathan, B.; Sastikumar, D.; Ramachandran, K.; *Adv. Sci. Lett*,**2012,** 5, 1. **DOI:** 10.1166/asl.2012.4259.
18. Pavan, M.; Ruhle, S.; Ginsburg,A.; Keller, D.A.; Barad, H.N.; Sberna, P.M.; Nunes, D.; Martins, R.; Anderson, A.Y.; Zaban, A.; Fortunato, E.; *Sol. Energ. Mat. Sol.***2015,** 132, 549. **DOI:** 10.1016/j.solmat.2014.10.005.
19. Zhang, L.; Jing, X.; Liu, J.; Wang, J.; Sun, Y.; *Sens. Actuators B,***2015.** **DOI:** 10.1016/j.snb.2015.07.113.
20. Wang, L.; Kang, Y.; Liu, X.; Zhang, S.; Huang, W.; Wang, S.; Sens. Actuators B, **2012**, 162, 237. **DOI:** 10.1016/j.snb.2011.12.073.
21. Mishra, Y.K.; Kaps, S.; Schuchardt, A.; Paulowicz, I.; Jin, X.; Gedamu, D.; Freitag, S.; Claus, M.; Wille, S.; Kovalev, A.; Gorb, S.N.; Adelung, R.; *Part. Part. Syst. Charact.***2013**, 30, 775. **DOI:** 10.1002/ppsc.201300197.
22. Jebril, S.; Kuhlmann, H.; Muller, S.; Ronning, C.; Kienle, L.; Duppel, V.; Mishra, Y.K.; Adelung, R.; *Crystal Growth & Design*, **2010**, 10, 2843. **DOI:** 10.1021/cg100538z.
23. Prabhu, M.; Mayandi, J.;Mariammal, R.N.;Vishnukanthan, V.; Pearce, J.M.;Soundararajan, N.;Ramachandran, K.;*Mater. Res. Express 2*,**2015**, 066202. **DOI:** 10.1088/2053-1591/2/6/066202.
24. Mishra, Y.K.; Modi, G.; Cretu, V.; Postica, V.; Lupan, O.; Reimer, T.; Paulowicz, I.; Hrkac, V.; Benecke, W.; Kienle, L.; Adelung, R.; *ACS Appl. Mater. Interfaces*,**2015**, 7, 14303. **DOI:** 10.1021/acsami.5b02816.
25. Kim, H.J.; Lee, J.H.; *Sens. Actuators B*, **2014**, 192, 607. **DOI:** 10.1016/j.snb.2013.11.005.
26. Nguyen, H.; El-Safty, S.A.; *J. Phys. Chem. C*,**2011**, 115, 8466. **DOI:** 10.1021/jp1116189.
27. Yan, N.; Hu, L.; Li, Y.; Wang, Y.; Zhong, H.; Hu, X.; Kong, X.; Chen, Q.; *J. Phys. Chem. C*,**2012**, 116, 7227. **DOI:** 10.1021/jp2126009.
28. Stella, C.; Soundararajan, N.; Ramachandran, K.; *AIP Adv.*, **2015**, 5, 087104. **DOI:** 10.1063 / 1.4928218.
29. Choi, U.S.; Sakai, G.; Shimanoe, K.; Yamazoe, N.; *Sens. Actuators B,***2004,** 98, 166. **DOI:** 10.1016/j.snb.2003.09.033.
30. Na, C.W.; Woo, H.S.; Kim, I.D.; Lee, J.H.; *Chem. Commun.*, **2011**,47,5148. **DOI:** 10.1039/c0cc05256f.
31. Sun, C.; Maduraiveeran, G.; Dutta, P.; *Sens. Actuators B,***2013,** 186, 117. **DOI:** 10.1016/j.snb.2013.05.090.
32. Lupan, O.; Cretu, V.; Postica, V.; Ababii, N.; Polonskyi, O.; Kaidas, V.; Schutt, F.; Mishra, Y.K.; Monaico, E.; Tiginyanu, I.; Sontea, V.; Strunskus, T.; Faupel, F.; Adelung, R.; *Sens. Actuators B,***2016**, 224, 434**.** **DOI:** 10.1016/j.snb.2015.10.042.
33. Xue, X.; Xing, L.; Chen, Y.; Shi, S.; Wang, Y.; Wang, T.; *J. Phys. Chem. C,***2008,** 112, 12157. **DOI:** 10.1021/jp8037818.
34. Hazra, S.K.; Basu, S.; *Sens. Actuators B,***2006,** 117, 177. **DOI:** 10.1016/j.snb.2005.11.018.
35. Park, S.; Kim, S.; Kheel, H.; Lee, C.; *Sens. Actuators B,***2016**, 222, 1193**.** **DOI:** 10.1016/j.snb.2015.08.006.
36. Yuan, J.; El-Sherif, M.A.; *IEEE Sens. J.*,**2003,** 3, 5. **DOI:** 10.1109/JSEN.2003.809023.
37. Mariammal, R.N.; Ramachandran, K.; Renganathan, B.; Sastikumar, D.; *Sens. Actuators B,***2012,** 169, 199. **DOI:** 10.1016/j.snb.2012.04.067.
38. Stella, C.; Soundararajan, N.; Ramachandran, K.; *J Mater Sci: Mater Electron*, **2015,** 26, 4178. **DOI:** 10.1007/s10854-015-2963-x.
39. Renganathan, B.; Sastikumar, D.; Gobi, G.; Yogamalar, N. R.; Chandra Bose, A.; *Sens. Actuators B,***2011,** 156, 263. **DOI:** 10.1016/j.snb.2011.04.031.
40. Singh, S.K.; Dhavale, V.M.; Kurungot, S.; *ACSAppl. Mater. Interfaces*,**2015**, 7, 21138. **DOI:** 10.1021/acsami.5b04865.
41. Kumar, M.; Kumar, A.; Abhyankar, A.C.; *ACS Appl. Mater. Interfaces*, **2015**, 7, 3571. **DOI:** 10.1021/am507397z.
42. Mariammal, R.N.; Stella, C.; Ramachandran, K.; AIP Conf. Proc., **2013**, 1512, 368. **DOI:** 10.1063/1.4791064.
43. Rajamanickam, N.; Mariammal, R.N.; Rajashabala, S.; Ramachandran, K.; *J. Alloys Compd.*, **2014**, 614, 151. **DOI:** 10.1016/j.jallcom.2014.06.081.
44. Ghosh, M.; Dilawar, N.; Bandyopadhyay, A.K.; Raychaudhuri, A.K; *J. Appl. Phys.*,**2009**, 106, 084306. **DOI:** 10.1063/1.3243341.
45. Song, W.T.; Xie, J.; Liu, S.Y.; Zheng, Y.X.; Cao, G.S.; Zhu, T.J.; Zhao, X.B.; *Int. J. Electrochem. Sci.*,**2012**, 7, 2164. **DOI:** http://www.electrochemsci.org/papers/vol7/7032164.pdf
46. Calizo, I.; Alim, K.A.; Fonoberov, V.A.; Krishnakumar, S.; Shamsa, M.; Balandin, A.A.; Kurtz, R.; *Proc. of SPIE*, **2007**, 6481, 64810N-1. **DOI:** 10.1117/12.713648.
47. Sharma, P.K.; Kumar, M.; Pandey, A.C.; *J Nanopart Res.*, **2011**, 13, 1629. **DOI:** 10.1007/s11051-010-9916-3.
48. Martin-Gonzalez, M.S.; Fernandez, J.F.; Rubio-Marcos, F.; Lorite, I.; Costa-Kramer, J.L.; Quesada, A.; Banares, M.A.; Fierro, J.L.G.; *J. Appl. Phys.*,**2008**, 103, 083905. **DOI:** 10.1063/1.2904862.
49. Serrano, A.; Pinel, E.F.; Quesada, A.; Lorite, I.; Plaza, M.; Perez, L.; Villacorta, F.J.; Venta, J.D.; Martin-Gonzalez, M.S.; Costa-Kramer, J.L.; Fernandez, J.F.; Llopis, J.; Garcia, M.A.; *Phys. Rev. B*, **2009**, 79, 144405. **DOI:** 10.1103/PhysRevB.79.144405.
50. Shafiu, S.; Kavas, H.; Baykal, A.; *J Supercond Nov Magn*.**2014**, 27, 1751. **DOI:** 10.1007/s10948-014-2506-3
51. Stella, C.; Diva, P.; Prabhu, M.; Soundararajan N.; Ramachandran, K.; *J Mater Sci: Mater Electron.*,**2015**. **DOI:** 10.1007/s10854-015-3935-x.
52. Mariammal, R.N.; Susila V.M.; Renganathan, B.; Sastikumar, D.; Ramachandran, K.; *SensorLett.*,**2012**,10,1. **DOI:** 10.1166/sl.2012.2318.
53. Liu, Y.; Zhu, G.; Chen, J.; Xu, H.; Shen, X.; Yuan, A.; *Appl. Surf. Sci.*,**2013**, 265, 379. **DOI:** 10.1016/j.apsusc.2012.11.016.
54. Bekermann, D.; Gasparotto, A.; Barreca, D.; Maccato, C.; Comini, E.; Sada, C.; Sberveglieri, G.; Devi, A.; Fischer, R.A.; *ACS Appl. Mater. Interfaces*,**2012**, 4, 928. **DOI:** 10.1021/am201591w.
55. Zhang, M.M; Jiang, G.S.; *Chin.J. chem.Phys.*,**2007**, 20, 315. **DOI:** 10.1088/1674-0068/20/03/315-318.

Supporting information

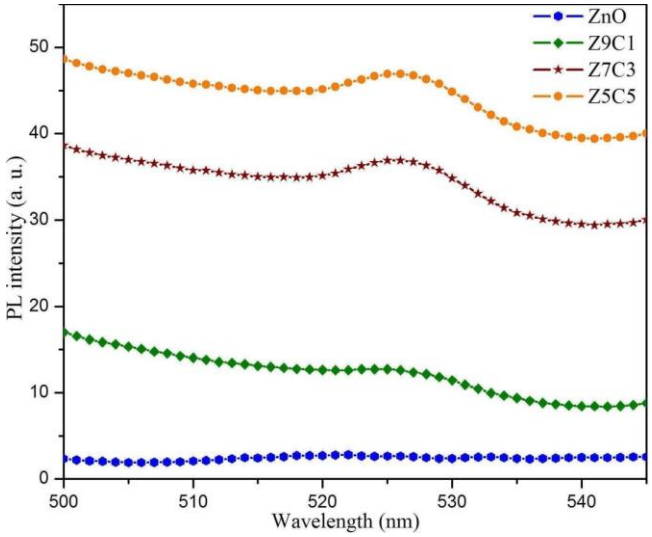

Fig. S1. (a) PL spectra of ZnO/Co_3O_4 nanocomposites.

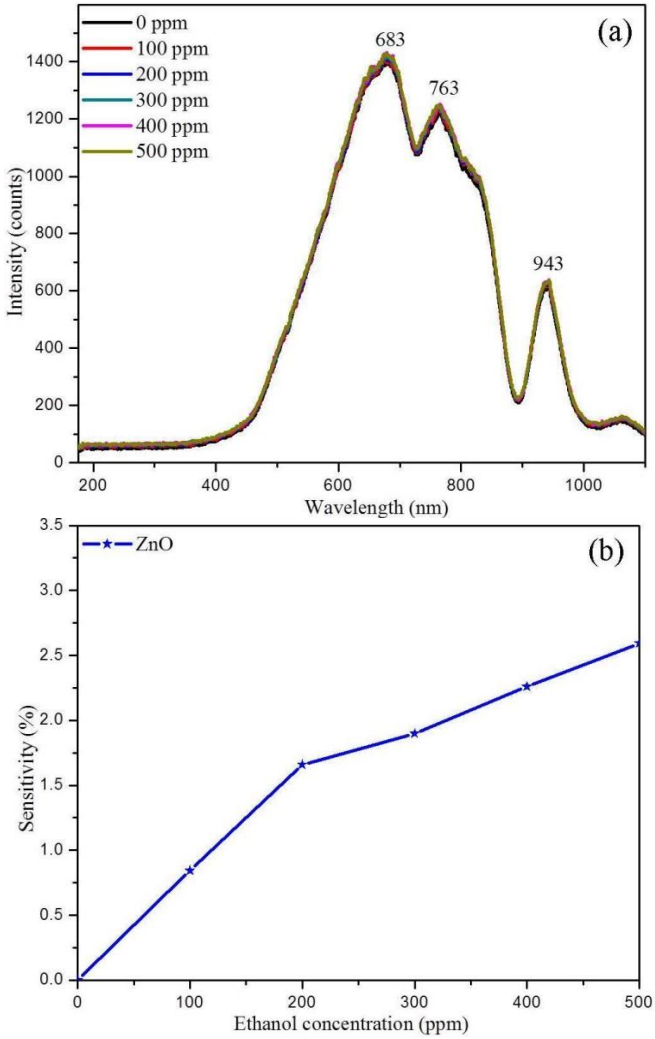

Fig. S2. (a) Spectral response, and (b) Variation of sensitivity with ethanol concentration for pure ZnO at RT.

